International Journal of Robotics and Control Systems
Vol. 5, No. 1, 2025, pp. 197-221
ISSN 2775-2658
http://pubs2.ascee.org/index.php/ijrcs

Performance Enhancement of Dual-Star Induction Machines Using Neuro-Fuzzy Control and Multi-Level Inverters: A Comparative Study with PI Controllers

Salah Eddine Mezaache [a,1,*], Elyazid Zaidi [b,2]

[a] ETA Laboratory, Department of Electronics, University Mohamed El Bachir El Ibrahimi of Bordj Bou Arreridj, Algeria
[b] Higher National School of Hydraulics (ENSH), Blida, Algeria
[1] s.mezaache@univ-bba.dz; [2] e.zaidi@ensh.dz
* Corresponding Author

ARTICLE INFO

Article history
Received October 10, 2024
Revised November 21, 2024
Accepted December 10, 2024

Keywords
Electrical Energy;
Dual Star Induction Motor;
Indirect Field Oriented Control;
Multi-Level Inverter;
Neuro-Fuzzy Controller

ABSTRACT

This paper proposes a hybrid speed control strategy for Dual-Star Induction Machines (DSIMs) supplied by Multi-Level Inverters (MLIs). The proposed approach integrates a Neuro-Fuzzy Controller (NFC) with an Indirect Field-Oriented Control (IFOC) technique, leveraging the adaptive learning capabilities of an Artificial Neural Network (ANN) to optimize the NFC parameters. This strategy achieves significant enhancements in speed regulation performance, including a 20% reduction in settling time, a 15% decrease in overshoot, and minimized steady-state error. The NFC's online adaptive learning capability enables real-time adjustments, outperforming the PI controller in handling rotor resistance variations and load disturbances. Simulation results demonstrate a 35% reduction in torque ripple and a 20% improvement in speed regulation compared to PI controllers. The NFC also exhibits faster response times during torque change and remains unaffected by 50% rotor resistance variations. Additionally, the NFC controller achieves up to 51% reduction in Total Harmonic Distortion (THD) compared to the PI controller. Increasing the inverter voltage level from m=2 to m=7 significantly reduces electromagnetic torque ripple, demonstrating a direct correlation between higher inverter levels and improved torque ripple performance. These improvements position the NFC-based strategy as a promising solution for industrial applications requiring precise speed control, such as robotics, electric vehicles, and automation systems.

1. Introduction

DSIMs powered by voltage source MLIs have emerged as a promising solution for a wide range of industrial applications. These machines offer several key advantages over traditional induction motors [1]-[4]. Their compact design enables higher power outputs in smaller physical footprints, leading to increased efficiency and reduced energy consumption. MLIs provide precise control over stator voltage and current, further enhancing efficiency and enabling more flexible operation (as depicted in Fig. 1) [1]-[3]. DSIMs can operate over a wide range of speeds, making them adaptable to varying load conditions. Additionally, their ability to regenerate energy during braking contributes to improved overall system efficiency and reduced energy costs. These combined benefits make DSIMs

an attractive choice for industries seeking high-performance, energy-efficient, and versatile electric motors.

The DSIM is designed with a unique stator configuration consisting of two spatially displaced six-phase windings [4]-[8]. These windings are divided into two three-phase sets, each connected in a wye configuration. The magnetic axes of the two sets are offset by an electrical angle $\alpha = 30°$ (Fig. 1) [8]. This arrangement allows for a more efficient use of space and provides additional flexibility in controlling the machine's performance. The rotor winding is a three-phase set that is uniformly distributed around the rotor, ensuring a balanced magnetic field and smooth operation.

Fault control of DSIMs presents several challenges due to their complex structure and operating characteristics. The presence of two stator windings can make fault detection and isolation more difficult compared to conventional three-phase machines [9]-[17]. Additionally, the interaction between the stator and rotor windings can amplify the effects of faults, making it challenging to accurately diagnose and mitigate their impact. Furthermore, the nonlinear nature of the DSIM's dynamics can introduce additional complexities in fault detection and control algorithms. These factors combined with the potential for high-frequency switching and transient phenomena in MLI-based drives can make fault control of DSIMs a demanding task, requiring robust and reliable fault detection and mitigation strategies [13], [14].

Conventional control algorithms, such as PI and PID controllers, while effective in many applications, suffer from well-documented limitations, including sensitivity to parameter variations, difficulty in handling nonlinear systems, and inability to adapt to changing operating conditions. These drawbacks necessitate the development of more sophisticated control methodologies [8], [18]-[21]. Therefore, electrical drives are subject to a range of electrical and mechanical faults, including inverter faults, machine faults, and sensor faults [22]-[28]. Therefore, maintaining uninterrupted operation of electrical drives, even in the presence of faults, is essential. To meet the stringent demands of high-performance induction machine drives, the implementation of intelligent controllers has become increasingly important [24].

Numerous approaches have been proposed as alternatives to traditional PI and PID control techniques. Among these, SMC is one of the most widely used and has received particular attention, leading to notable advancements in the control of multiphase machines, especially six-phase induction machines [29], [30]. Early work by [31] integrated SMC with fuzzy logic for robust control under both healthy and faulty conditions. In [32], the authors use an SMC controller to improve the performance and robustness of a DSIM drive system fed by two multilevel inverters, showing better disturbance rejection and reduced harmonic distortion. However, to implement a control scheme on a sampled-data, the discrete-time sliding mode control (DSMC) is preferable [33]. To improve the results obtained with the DSMC, a Time Delay Estimation (TDE)-based DSMC has been developed for multiphase Induction Motor (IM) drive [34]. To mitigate chattering, many approaches have been implemented for multiphase machines. The authors in [35] introduced a DSMC with an exponential reaching law, Discrete-time Super-Twisting Algorithm (DSTA) has been applied to the six phase machine in [34] and Discrete-time Terminal STA (DTSTA) [36]. Also, Higher Order Sliding Mode Controller (HOSMC) that extends the principles of classical SMC to higher-order derivatives of the sliding surface, has been successfully applied to multiphase machines [37]. This approach, by acting on higher-order derivatives, achieves finite-time convergence to the sliding surface, offering advantages such as reduced chattering, improved accuracy, faster convergence, and enhanced system performance and robustness [34], [38]. Otherwise, some works presented combinations of sliding mode with other techniques such as fuzzy logic, neural networks or both.

Fuzzy logic control, known for its adaptability and minimal need for precise mathematical modeling, has also been applied effectively in multiphase systems [31], [39]-[43]. This controller operates based on fuzzy theory, using linguistic rules that emulate human reasoning as the foundation of its design. Various methods have been used to design fuzzy logic speed controllers in motor drives. However, a basic fuzzy controller applied to machine drive speed control typically exhibits limited

effectiveness across a restricted operating range, requiring extensive manual fine-tuning to attain optimal performance [8]. In [44], fuzzy logic-based pitch angle control strategy was proposed, using the generator's output power and speed as reference parameters to determine the pitch angle via a fuzzy logic controller (FLC). Authors in [45] introduces an advanced control strategy that balances power flow between wind turbines and the power load center using fuzzy logic controller. In [46], authors proposed an implementation of effective rotor current control schemes for DSIG based PI, FLC, and fuzzy-PI to maximize the electric power production efficiency along with enhancing the system's response. In [47], IFOC with fuzzy logic controllers (FLC) is used to control the rotor currents and consequently the real and reactive powers of the stator generator to improve the energy quality extracted by variable speed wind turbine based on doubly fed induction generator.

Some methods combined the features of FLC with other model like SMC or back-stepping in order to enhance the drive performance under heavy motor parameters variations and various operating ranges [48]. Nevertheless, the use of other mechanisms increases the system's computational burden [41].

Back-stepping control offers another promising approach by systematically designing stabilizing feedback for nonlinear systems, as evidenced by several successful implementations [49]-[53]. The major drawback of the back-stepping control is the iterative design process which require a deep understanding of system dynamics and mathematic formulation and involve high demand on computational resources [54].

Artificial Neural Networks (ANNs) have emerged as a powerful tool for controlling induction motors due to their ability to learn complex nonlinear relationships and adapt to varying operating conditions [55]. Many ANN based control strategies have been proposed [56], [57], [19], [4], [55]. In [58], the authors proposed a neural network-based DTC control system to operate under open switch faults. They demonstrate improved performance even in faulty conditions. In [59], authors use an ANN controller trained offline by extracting data from Direct Thrust Control (DTC) to suppress current ripples. The fusion of various artificial intelligence techniques, known as Hybrid Control, has recently gained significant attention in scientific and engineering fields. Studies have shown that combining multiple methods consistently outperforms single-technique approaches in model performance [60].

The contribution of this paper is to investigate the use of a neuro-fuzzy controller (NFC) for a DSIM powered by two MLI. It hybridizes the FLC with the ANN and maintain a simple structure, showing robustness to disturbances, and precise speed tracking. Furthermore, the use of MLI to power the DSIM with the NFC led to a constant output voltage and confirm the effectiveness of the proposed controller. This hybrid controller has the ability to adapt to any situation, such as the load change and inverter fault. The main focus of the study was achieved through simulation in MATLAB/SIMULINK software and the analysis of the results.

2. NFC System Design

2.1. DSIM Modeling

The DSIM, as shown in Fig. 1 [61], [3], [32], consists of two stators that are offset by an electrical angle and a mobile squirrel cage rotor. Each stator is composed of three stationary windings. This configuration allows for enhanced control and performance compared to conventional single-stator induction motors. Fig. 1 illustrates the DSIM's winding arrangement, providing a clear visual representation of its structure.

The stator of the DSIM is configured with six phases, divided into two wye-connected three-phase sets, labeled S_{a1}, S_{b1}, S_{c1} and S_{a2}, S_{b2}, S_{c2}, with their magnetic axes offset by an electrical angle of 30°. Each three-phase set has uniformly distributed windings, with axes separated by 120°. The rotor is squirrel cage consisting of conduction bars short-circuited by a conductive ring at each

end, and they simulated as three-phase windings (R_a, R_b, R_c) sinusoidally distributed and have axes that are displaced by 120°apart.

To simplify the analysis of DSIMs, several assumptions are commonly made: sinusoidal winding distributions, identical parameters for both stator winding sets, linear magnetic flux paths, and the inclusion of mutual leakage inductances. These simplifications allow for a more tractable mathematical model, facilitating analysis and control design [3], [61]-[63]. In effect, assuming identical winding parameters simplifies calculations, although it may not accurately reflect conditions such as temperature variations or winding degradation. Nevertheless, their influence on the overall system performance (torque, flux, and speed control) is minimal, especially under nominal operating conditions.

2.2. Mathematical Model of DSIM

Taking into account the simplifying assumptions mentioned above, and applying the Park transformation (Fig. 2) to the three-phase model of the DSIM (Fig. 1), we obtain the following equation system, expressed in the (d,q) reference frame [48], [64], [65]:

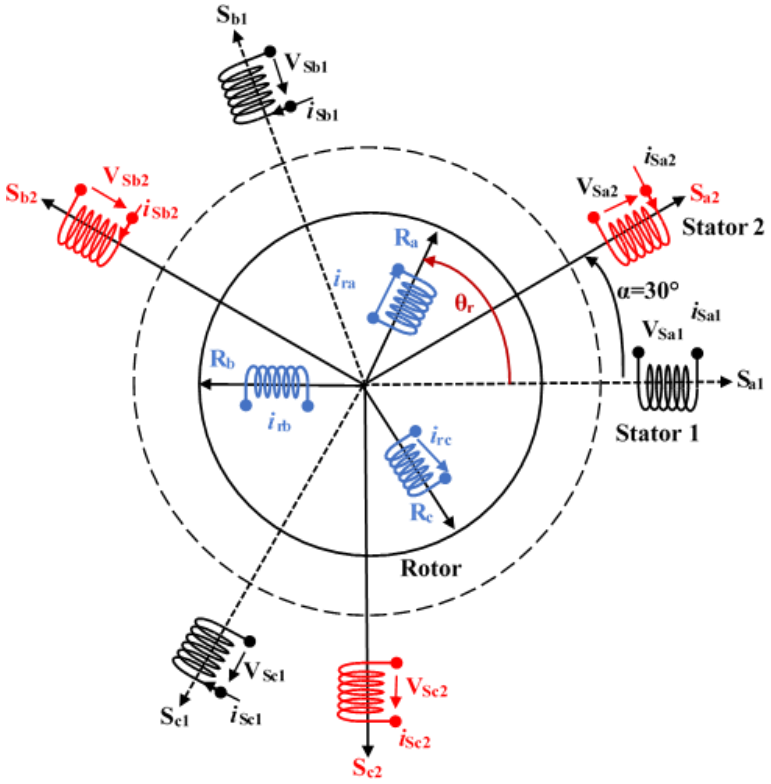

Fig. 1. Schematic representation of dual star induction machine (DSIM)

2.2.1. Equation for the Stator and Rotor Voltages

$$\begin{cases} V_{ds1} = R_s i_{ds1} + \dfrac{d\Phi_{ds1}}{dt} - \omega_s \Phi_{qs1} \\ V_{qs1} = R_s i_{qs1} + \dfrac{d\Phi_{qs1}}{dt} + \omega_s \Phi_{ds1} \end{cases} \quad (1)$$

$$\begin{cases} V_{ds2} = R_s i_{ds2} + \dfrac{d\Phi_{ds2}}{dt} - \omega_s \Phi_{qs2} \\ V_{qs2} = R_s i_{qs2} + \dfrac{d\Phi_{qs2}}{dt} + \omega_s \Phi_{ds2} \end{cases} \quad (2)$$

And the equation for the rotor voltages:

$$\begin{cases} 0 = R_r i_{dr} + \dfrac{d\Phi_{dr}}{dt} - (\omega_{s-}\omega_{r)}\lambda_{qr} \\ 0 = R_r i_{qr} + \dfrac{d\Phi_{qr}}{dt} + (\omega_{s-}\omega_{r)}\lambda_{dr} \end{cases} \quad (3)$$

Where V_{ds1}, V_{qs1}, V_{ds2}, and V_{qs2} : stator voltages $d-q$ axis components; i_{ds1}, i_{qs1}, i_{ds2}, and i_{qs2}: stator currents $d-q$ axis components and Φ_{ds1}, Φ_{qs1}, Φ_{ds2}, and Φ_{qs2}: stator flux $d-q$ axis components. R_s: stator resistance and ω_s: the speed of the synchronous reference frame. i_{dr} and i_{qr} : rotor currents $d-q$ axis components, Φ_{dr} and Φ_{qr} rotor flux $d-q$ axis components. R_r: rotor resistance and ω_s, ω_r : speed of synchronous reference frame and rotor electrical angular respectively.

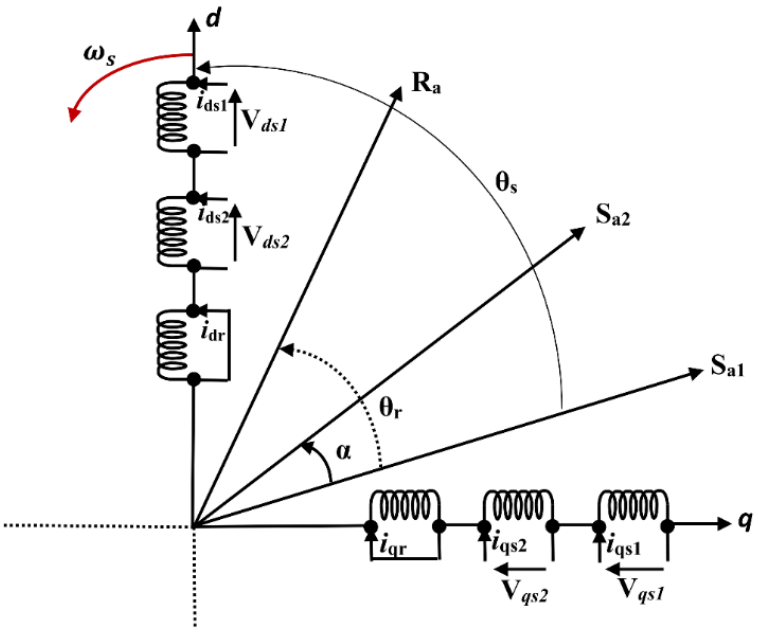

Fig. 2. Model of the DSIG in the park frame

2.2.2. Magnetic Equation for the Rotor and the Stator Flux Linkages

$$\begin{cases} \Phi_{ds1} = L_s i_{ds1} + L_m(i_{ds1} + i_{ds2} + i_{dr}) \\ \Phi_{qs1} = L_s i_{qs1} + L_m(i_{qs1} + i_{qs2} + i_{qr}) \end{cases} \quad (4)$$

$$\begin{cases} \Phi_{ds2} = L_s i_{ds2} + L_m(i_{ds1} + i_{ds2} + i_{dr}) \\ \Phi_{qs2} = L_s i_{qs2} + L_m(i_{qs1} + i_{qs2} + i_{qr}) \end{cases} \quad (5)$$

$$\begin{cases} \Phi_{dr} = L_r i_{dr} + L_m(i_{ds1} + i_{ds2} + i_{dr}) \\ \Phi_{qr} = L_r i_{qr} + L_m(i_{qs1} + i_{qs2} + i_{qr}) \end{cases} \quad (6)$$

Where L_m: cyclic mutual inductance between stator (1, 2); and rotor and L_s, L_r: the inductance of stator (1, 2), and rotor respectively.

2.2.3. Mechanical and Electromagnetic Torque Equation

The mechanical dynamics of a DSIM can be described by the mechanical equation expressed by (7), where the equation of the electromagnetic torque is given by (8):

$$J\frac{d\omega_r}{dt} = C_{em} - C_r - f\omega_r \quad (7)$$

$$C_{em} = P\frac{L_m}{L_m + L_r}\left(\Phi_{dr}\left(i_{qs1} + i_{qs2}\right) - \Phi_{qr}\left(i_{qs1} + i_{qs2}\right)\right) \quad (8)$$

Where J: moment of inertia of the rotor; C_{em}: electromagnetic torque; C_r: load torque; f: friction coefficient and P: number of pole pairs.

3. Indirect Field Oriented Control (IFOC)

3.1.1. Concept of IFOC

Indirect Field-Oriented Control (IFOC) is a technique that enables precise control of rotor flux and electromagnetic torque in an induction machine, analogous to the control of a DC motor, by decoupling flux and torque control. By aligning the stator current with the rotor flux, IFOC allows for independent control of both flux and torque in AC machines [66]. It consists of annulling the quadrature component of the rotor flux $\Phi_{qr} = 0$ while the rotor direct flux converges to the reference flux ($\Phi_{dr} = \Phi_r^*$) [3].

The indirect vector controller is derived from the dynamic equation of the machine in the synchronously rotating reference frame ($\omega_s = \omega_b$), with ω_b is rotor flux vector angular velocity.

3.1.2. Derivation of IFOC Scheme

We can derive the new rotor voltage equations from (3) considering $\frac{d\Phi_{qr}}{dt} = 0$

$$\begin{cases} 0 = R_r i_{dr} + \dfrac{d\Phi_{dr}}{dt} \\ 0 = R_r i_{qr} + \omega_{sl}\Phi_{dr} \end{cases} \quad (9)$$

Where $\omega_{sl} = \omega_b - \omega_r$ is the Slip speed.

The rotor currents in terms of the stator currents are derived from (6) as

$$i_{dr} = \left(\frac{\Phi_r^*}{L_r}\right) - \left(\frac{L_m}{L_r}\right)\left(i_{ds1} + i_{ds2}\right) \quad (10)$$

$$i_{qr} = \left(\frac{-L_m}{L_r}\right)\left(i_{qs1} + i_{qs2}\right) \quad (11)$$

Substituting both quadrature and direct rotor currents from (10) and (11) into (9), we obtain:

$$i_{ds}^* = \left(\frac{1}{L_m}\right)\Phi_r^* + \left(\frac{T_r}{L_m}\right)\frac{d\Phi_r^*}{dt} \quad (12)$$

$$i_{qs}^* = \frac{1}{P}\left(\frac{L_r}{L_m}\right)\frac{C_{em}^*}{\Phi_r^*} \quad (13)$$

$$_{\text{sl}} = \left(\frac{L_m}{T_r}\right)\frac{i_{\text{qs}}}{\Phi_r^*} \quad (14)$$

Where:$T_r = \frac{L_r}{R_r}$ denotes the rotor time constant. The $d-$ and $q-$ axes currents i_{ds}^* and i_{qs}^* are the flux-producing and torque-producing components of the stator current respectively.

$$i_{qs}^* = i_{qs1}^* + i_{qs2}^* \quad (15)$$

$$i_{ds}^* = i_{ds1}^* + i_{ds2}^* \quad (16)$$

Similarly, by substituting the rotor currents from equations (10) and (11) into the torque expression, the electromagnetic torque can be expressed as:

$$C_{em}^{*} = P\left(\frac{L_m}{L_r}\right)\Phi_r^{*} i_{qs}^{*} \tag{17}$$

The slip angle θ_{sl} is obtained by integrating the slip speed ω_{sl}.

The commands/references voltages are derived by substituting the equation (10) and (11) in (1) and (2):

$$\begin{cases} V_{ds1}^{*} = R_s i_{ds1} + l_s \dfrac{d}{dt} i_{ds1} - \omega_s^{*}\left(l_s i_{qs1} + T_r \Phi_r^{*} \omega_{sl}^{*}\right) \\ V_{qs1}^{*} = R_s i_{qs1} + l_s \dfrac{d}{dt} i_{qs1} + \omega_s^{*}\left(l_s i_{ds1} + \Phi_r^{*}\right) \end{cases} \tag{18}$$

$$\begin{cases} V_{ds2}^{*} = R_s i_{ds2} + l_s \dfrac{d}{dt} i_{ds2} - \omega_s^{*}\left(l_s i_{qs2} + T_r \Phi_r^{*} \omega_{sl}^{*}\right) \\ V_{qs2}^{*} = R_s i_{qs2} + l_s \dfrac{d}{dt} i_{qs2} + \omega_s^{*}\left(l_s i_{ds2} + \Phi_r^{*}\right) \end{cases} \tag{19}$$

3.1.3. Implementation of Indirect Vector Control Scheme

Fig. 3 illustrates the proposed NFC control process with IFOC for a DSIM drive supplied by two MLIs. The IFOC controller takes speed and flux demands as inputs and produces the corresponding reference values for the torque- and flux-producing components of the stator current i_q^{*} and i_d^{*}. It consists of cascaded control loops and an angle calculation block for θ_s. The inner loops regulate the $d-$ axis and $q-$ axis stator currents, I_{sd} and I_{sq}, while the outer loop manages the rotor speed Ω.

The output of the speed controller provides the reference for the electromagnetic torque or the $q-$ axis current I_{sq}^{*}. Similarly, the flux control loop generates the reference for the d-axis current I_{sd}^{*}.

Finally, the two reference voltages,V_{sd}^{*} and V_{sq}^{*} , obtained from the current controllers, are transformed into the stator reference frame using the calculated angle θ_s. A Park reverse transformation $(dq-abc)$ calculates the stator reference voltages. These voltages are used to fix the control of each PWM inverter. Additionally, the voltage references V_{sd} and V_{sq} may include static decoupling terms added to the output of the current controllers to enhance dynamic performance.

3.2. DSIM Neuro-Fuzzy Controller

The NFC system employs a neuro-fuzzy network, trained through an advanced online learning algorithm, as illustrated in Fig. 4. The controller accept a reference speed Ω^{*} and compare it to the actual measured speed Ω_m to generate an error e_ω. This error is used by a PI controller to generate the reference torque C_{em}^{*}. Furthermore, the error e_ω and its derivative $\frac{d}{dt}e_\omega$ noted e_ω^{*} in the block diagram are used as input to the NFC controller to generate torque command output [43], [64], [67]. At the beginning, the PI controller generate the reference torque C_{em}^{*} which is compared to the one generated by the NFC controller noted $C_{(em-NFC)}$, the error $e_{C_{em}}$ is used to adjust the torque generated by the NFC controller $C_{(em-NFC)}$. The online learning algorithm continuously updates the neuro-fuzzy network's parameters based on the feedback and error signals, allowing the system to adapt to changes in motor load, or variations in motor characteristics. The backpropagation algorithm operates in an online learning mode, continuously updating parameters based on incoming data. The bloc of Field Weakening generates the reference flux Φ_r^{*}. The ANN architecture, illustrated in Fig. 5, consists of four layers: input, fuzzification, rule evaluation, and defuzzification.

The fuzzification, inference mechanism, and defuzzification are parts of the fuzzy logic controller. Then, neural network approaches are used to enhance its performance.

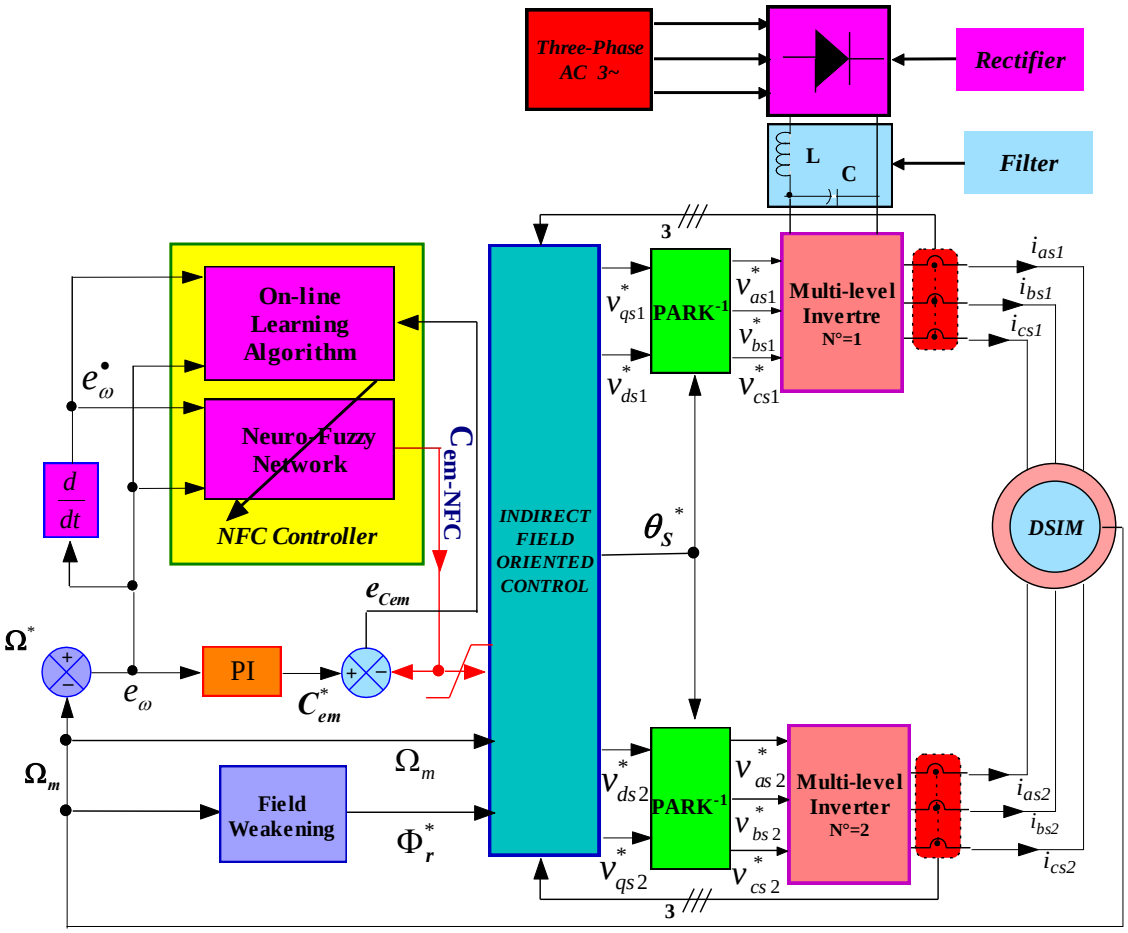

Fig. 3. Block diagram of neuro-fuzzy for speed control of IFOC-DSIM

3.2.1. Design of Fuzzification and Membership Functions

Input layer: Each input node in this layer corresponds to the specific input variable. The inputs of this layer are given by $N_1^{L1} = e_\omega$ and $N_2^{L1} = e_\omega^*$ with N_j^{L1} refer to the input number j of the network layer 1. The outputs of this layer are given by:

$$\begin{cases} y_1^{L1} = f_1^{L1}(N_1^{L1}) = e_\omega \\ y_2^{L1} = f_2^{L1}(N_2^{L1}) = e_\omega^* \end{cases} \quad (20)$$

The weights of this layer are unity and fixed.

Fuzzification layer: referred as the fuzzification procedure. Each node in the fuzzification layer represents a Gaussian membership function that transforms a crisp input into a fuzzy degree of membership. In this system, seven Gaussian membership functions are used to represent seven fuzzy categories (Table 1), allowing the system to classify inputs across these categories as shown in Fig. 6.

Table 1. Linguistic variables used in the fuzzification procedure

Description of the linguistic term	Acronym
Negative Small	NS
Negative Medium	NM
Negative Big	NB
Zero Environ	ZE
Positive Small	PS
Positive Medium	PM
Positive Big	PB

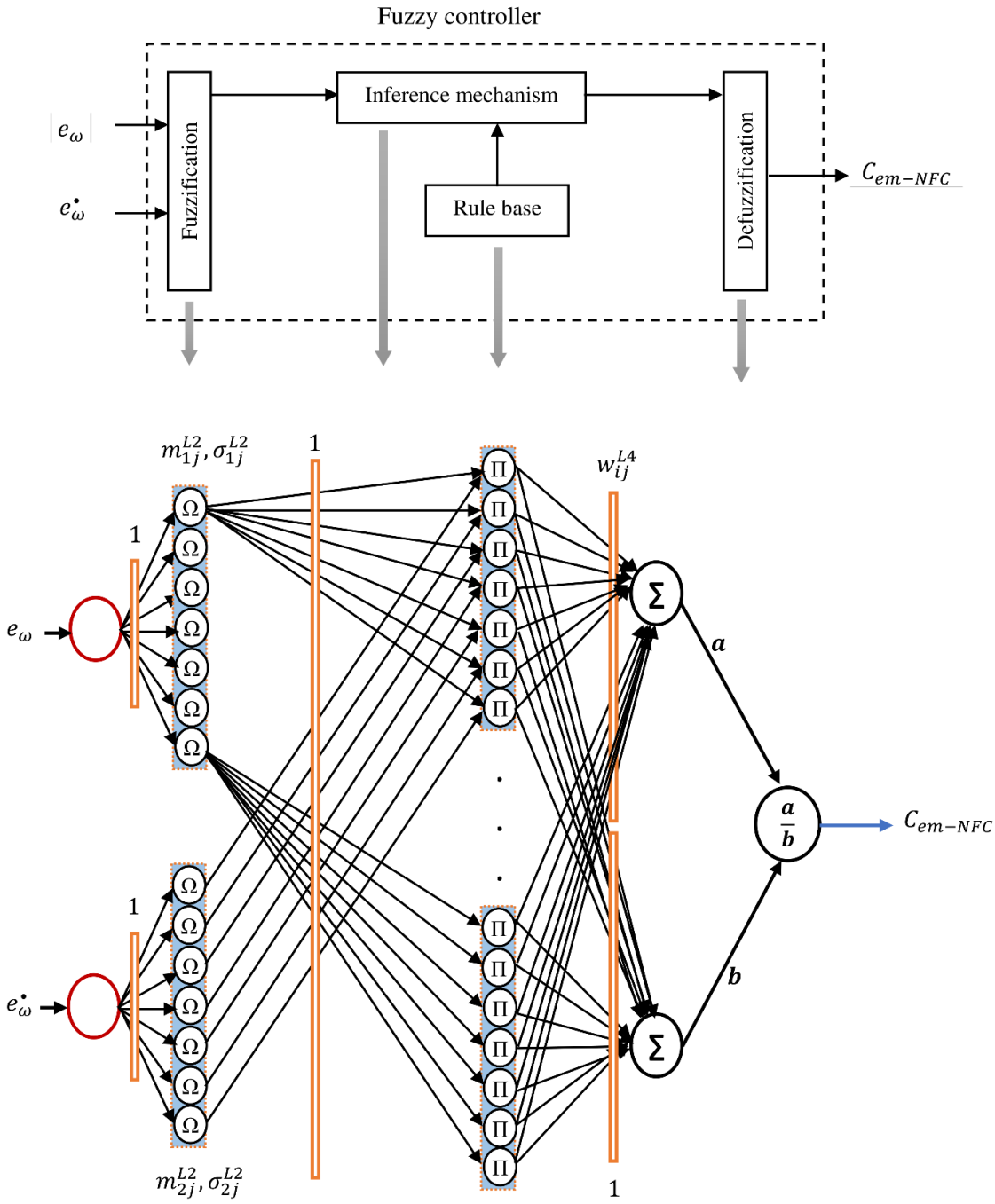

Fig. 4. Block diagram of the proposed neuro-fuzzy controller, e_ω, e_ω^*: error and change of error of the motor speed; $m_{1j}^{L2}, m_{2j}^{L2}, \sigma_{1j}^{L2}$, σ_{2j}^{L2}: mean and width of the Gaussian functions of e_ω, e_ω^* respectively; w_{ij}^{L4}: weights related to m

The outputs of the fuzzification procedure are given as follows.

$$N_{1,j}^{L2} = -\left(\frac{x_{1,j}^{L2} - m_{1,j}^{L2}}{2\sigma_{1,j}^{L2}}\right)^2 \tag{21}$$

$$N_{2,j}^{L2} = -\left(\frac{x_{2,j}^{L2} - m_{2,j}^{L2}}{2\sigma_{2,j}^{L2}}\right)^2 \tag{22}$$

$$\begin{cases} y_{1,j}^{L2} = f_{1,j}^{L2}\left(N_{1,j}^{L2}\right) = e^{N_{1,j}^{L2}} \\ y_{2,j}^{L2} = f_{2,j}^{L2}\left(N_{2,j}^{L2}\right) = e^{N_{2,j}^{L2}} \end{cases} \quad (23)$$

Where: $m_{1j}^{L2}, m_{2j}^{L2}, \sigma_{1j}^{L2}, \sigma_{2j}^{L2}$: mean and width of the Gaussian functions of e_ω, e_ω^* respectively.

The result of the fuzzification process is a set of membership degrees for each fuzzy set, providing a fuzzy representation of the input.

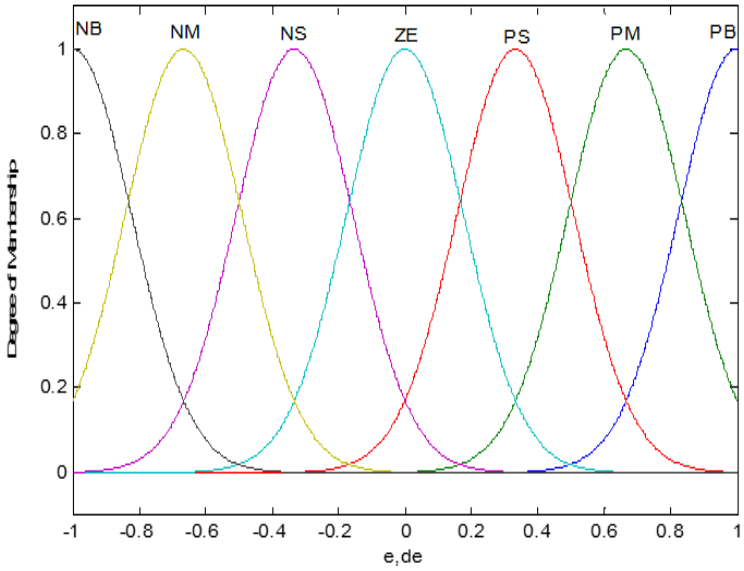

Fig. 5. Membership functions for inputs "e" and "de"

3.2.2. Inference Mechanism and Rule Base Design

The inference mechanism, guided by a rule base that defines input-output relationships, employs approximate reasoning to make decisions within the fuzzy controller.

Rule layer: In this layer, each node represents a fuzzy rule. The output of a node is calculated by multiplying the outputs of its connected nodes in the previous layer. The neuro-fuzzy controller utilizes a rule base consisting of 49 rules, as depicted in Table 2. The values of weights between second layer and third layer are unity.

Table 2. Rules base for FLC controller

e \ Δe	NB	NM	NS	ZE	PS	PM	PB
PB	ZE	NS	NM	NB	NB	NB	NB
PM	PS	ZE	NS	NM	NB	NB	NB
PS	PM	PS	ZE	NS	NM	NB	NB
ZE	PB	PM	PS	ZE	NS	NM	NB
NS	PB	PB	PM	PS	ZE	NS	NM
NM	PB	PB	PB	PM	PS	ZE	NS
NB	PB	PB	PB	PB	PM	PS	ZE

3.2.3. Defuzzification

The defuzzification process converts the fuzzy output from the inference mechanism into a crisp signal. Various methods are available to transform the inference mechanism's conclusion into the final output of the fuzzy controller.

Defuzzification layer: The proposed controller utilizes the "center of gravity" method to aggregate the outputs of individual fuzzy rules. This method calculates the centroid of the possibility distribution, yielding the final control actions, a and b.

$$\begin{cases} a = \sum_j \sum_k w_{jk}^{L4} y_{jk}^{L3} \\ b = \sum_j \sum_k y_{jk}^{L3} \end{cases} \quad (24)$$

$$N_o^{L4} = \frac{a}{b}, \qquad y_o^{L4} = f_o^{L4}(N_o^{L4}) = \frac{a}{b} \quad (25)$$

y_{ij}^{L3} : specify the values of the output membership functions used in the FLC, w_{ij}^{L4}: the weights of the third layer, N_0^{L4}: the output of the defuzzification layer. $\boldsymbol{a}$ and $\boldsymbol{b}$ are the numerator and the denominator of the function used in the center of area technique, respectively.

3.2.4. Back Propagation Algorithm

The goal of the learning algorithm is to reduce the error, which represents the difference between the desired output (target) and the actual output produced by the controller. This is achieved by fine-tuning the parameters of the fuzzy membership functions and the rule weights, which determine how input variables are mapped to output actions.

In this work, the supervised gradient descent method is used as a learning algorithm in NFC to adjust the parameters of fuzzy membership functions and rule weights, allowing the system to adaptively learn from input-output data.

The error function represents the difference between the desired output and the actual output of the NFC, i.e., (The desired torque C_{em}^*, and the actual torque produced by the NFC C_{em-NFC}^*) . The least-mean-square (LMS) algorithm, based on the concept of the stochastic approximation method, is used to minimize the criterion function given in equation (26).

$$E = \frac{1}{2}(C_{em}^* - C_{em-NFC}^*)^2 \quad (26)$$

The generalized delta rule uses the chain rule of differentiation to calculate the error gradient for each parameter in the network. Thus, the parameters would be adapted as.

$$Z(t+1) = Z(t) - \tau \frac{\partial E}{\partial Z} \quad (27)$$

Here, Z represents the parameter to be adapted; τ is the learning rate; $Z(t)$ denotes the parameter vector Z at iteration t; and t indicates the iteration count. Therefore, the equations governing the parameter adaptation are:

$$m_{ij}^{L2}(t+1) = m_{ij}^{L2}(t) - \tau_m \frac{\partial E}{\partial m_{ij}^{L2}} \quad (28)$$

$$\sigma_{ij}^{L2}(t+1) = \sigma_{ij}^{L2}(t) - \tau_\sigma \frac{\partial E}{\partial \sigma_{ij}^{L2}} \quad (29)$$

$$w_{ij}^{L4}(t+1) = w_{ij}^{L4}(t) - \tau_w \frac{\partial E}{\partial w_{ij}^{L4}} \quad (30)$$

The partial derivative of E with respect to the network's output y is:

$$\frac{\partial E}{\partial y} = -(y_d - y_o^{L4}) \quad (31)$$

Where, y_d is the desired output (C_{em}^*).

The defuzzification layer computes the output as:

$$y_o^{L4} = \frac{\sum w_{ij}^{L4} \cdot y_{ij}^{L3}}{\sum y_{ij}^{L3}} \tag{32}$$

The derivative of y_o^{L4} with respect to w_{ij}^{L4} is:

$$\frac{\partial y_o^{L4}}{\partial w_{ij}^{L4}} = \frac{y_{ij}^{L3}}{\sum y_{ij}^{L3}} = \frac{y_{ij}^{L3}}{b} \tag{33}$$

The generalized delta rule for w_{ij}^{L4} is:

$$\frac{\partial E}{\partial w_{ij}^{L4}} = \frac{\partial E}{\partial y_o^{L4}} \cdot \frac{\partial y_o^{L4}}{\partial w_{ij}^{L4}} \tag{34}$$

The update rule is:

$$w_{ij}^{L2}(t+1) = w_{ij}^{L2}(t) + \tau_w \cdot e \cdot \frac{y_{ij}^{L3}}{b} \tag{35}$$

τ_w is the learning rate for the weights. w_{ij}^{L4}.

The generalized delta rule for m_{ij} requires the chain rule:

$$\frac{\partial E}{\partial m_{ij}} = \frac{\partial E}{\partial y_o^{L4}} \cdot \frac{\partial y_o^{L4}}{\partial y^{L2}} \cdot \frac{\partial y^{L2}}{\partial m_{ij}} \tag{36}$$

Where:

$$\frac{\partial y_{ij}^{L2}}{\partial m_{ij}} = y_{ij}^{L2} \cdot \frac{\left(x_{ij} - m_{ij}\right)}{\sigma_{ij}^2} \tag{37}$$

The error received from the output, then the rule layer yield to:

$$m_{ij}^{L2}(t+1) = m_{ij}^{L2}(t) + \tau_m \frac{e}{b} \frac{\left(x_{ij}^{L2} - m_{ij}^{L2}\right)}{\left(\sigma_{ij}^{L2}\right)^2} \sum_k \left(w_{jk}^{L4} - y_d\right) y_{jk}^{L3} \tag{38}$$

$$\sigma_{ij}^{L2}(t+1) = \sigma_{ij}^{L2}(t) + \tau_\sigma \frac{e}{b} \frac{\left(x_{ij}^{L2} - m_{ij}^{L2}\right)^2}{\left(\sigma_{ij}^{L2}\right)^3} \sum_k \left(w_{jk}^{L4} - y_d\right) y_{jk}^{L3} \tag{39}$$

3.3. Multi-Level Inverter Design

Multilevel inverters (MLIs) are designed with a modular structure, allowing easier scaling and customization, and they are also fault-tolerant, meaning they can continue to operate even if some components fail. They provide smoother waveforms, which reduces unwanted harmonics (distortions in the signal) and minimizes the stress on electronic components during switching.

First developed by Baker and Bannister in 1975, the Cascaded H-Bridge (CHB) topology connects multiple full-bridge cells with isolated DC supplies to create multilevel output voltages [68]. Later advancements in MLI topologies include the diode-clamped (NPC) inverter introduced by Nabae and Akagi in 1981, which uses diodes and capacitors to produce multiple voltage levels [69],

and the flying capacitor (FC) inverter developed by Meynard and Foch in 1992, which relies on capacitors for voltage clamping [70]. These topologies are widely used in industrial applications, such as electric vehicles, grid-connected solar systems, industrial drives, and medical equipment [71].

The Cascaded H-Bridge (CHB) inverter has gained significant attention among multilevel inverters due to its modularity and effectiveness. For AC high-power applications, the NPC (Neutral Point Clamped) converter is commonly used, especially in the 2.3 kV to 6 kV range, and is well-suited for back-to-back power flow applications. In NPC converters, a single DC source is divided by multiple DC-link capacitors [72], and unidirectional current flow requires a large number of clamping diodes. As the number of levels increases, the voltage stress on the power diodes also rises, with limited redundant states available [73].

The CHB inverter, however, does not require additional clamping diodes or capacitors, making it a preferred choice among multilevel converters. Despite these advantages, the CHB topology has some challenges: achieving higher output levels requires an increased number of power switches, which leads to larger installation space, more gate driver circuits, and higher overall costs [27], [71]. An outlook on the development of various topologies of MLI is provided in reference [71].

3.3.1. Topology of CHB Inverter

The Cascaded H-Bridge Multilevel Inverter (CHB-MLI) operates by combining multiple H-bridge cells, each powered by an independent DC voltage source. Each H-bridge cell within the CHB-MLI generates three possible voltage levels: zero, positive DC, and negative DC. By carefully controlling the switching states of each cell, the inverter produces a staircase waveform that approximates a sinusoidal output. The overall output voltage is the sum of the voltages produced by each H-bridge cell. When the CHB-MLI has m H-bridge cells, it can generate a total of $2m + 1$ distinct voltage levels [71].

In this work, the proposed structure is a multilevel, three-phase cascaded H-bridge inverter, where each phase leg includes a series-connected H-bridge cell. This configuration, as shown in the Fig. 6 for the seven level configuration, uses standard three-leg converters combined with H-bridge cells per phase. The three identical H-bridge cells connected in parallel, each corresponding to one phase of a three-phase system (phases V_a, V_b, and V_c). Each H-bridge cell consists of four switches (labeled S_a, S_b, S_c and S_d for each phase) and generates three voltage levels: ${V_{dc}}/{2}$, 0, ${-V_{dc}}/{2}$ when switches $S_a - S_d$, $S_a - S_b$ or $S_c - S_d$, and $S_c - S_b$ are turned ON, respectively.

3.3.2. Control And Modulation Strategies

Modulation techniques are essential for regulating the inverter, as they directly affect critical efficiency parameters such as harmonic reduction and switching losses, thereby shaping the overall performance of the entire system. The modulation methods used in multilevel inverters can be classified according to switching frequency, as shown in Fig. 7.

In this work, Multi-Carrier Pulse Width Modulation (MC-PWM) is used to control the switching of the active components. The technique involves comparing multiple triangular carrier signals with a reference (or modulating) signal (for each phase) with the desired frequency to control the switching of the inverter's power devices (Fig. 8). The points where the carrier and reference waves intersect determine the switching instants and generate the modulated pulse signals.

The proposed technique uses Level-Shifted Phase Disposition PWM, where carrier signals are aligned vertically and in phase, with each level corresponding to a different voltage level of the inverter. The carrier frequency is set to 10 kHz. Fig. 8 shows the typical voltage generated by one cell for the inverter.

4. Simulation Results

To demonstrate the effectiveness of the proposed neuro-fuzzy controller, simulations using a DSIM fed by two CH-MLI's are performed. The DSIM employed in this study was a four-pole,

230/380V, 6A, 4.5KW, and 2753 rpm. The nominal values of the parameters used in the simulations are listed in the Appendix (Table 4). The drive system was tested with a step reference speed of 2500 rpm, and its performance was analyzed under step variations in load torque and robustness against parameter variations. Specially, the rotor resistance, which varies with load and ambient temperature, is tested under a scenario of a 50% increase to evaluate the impact of DSIM parameter variations on the performance of the proposed NFC.

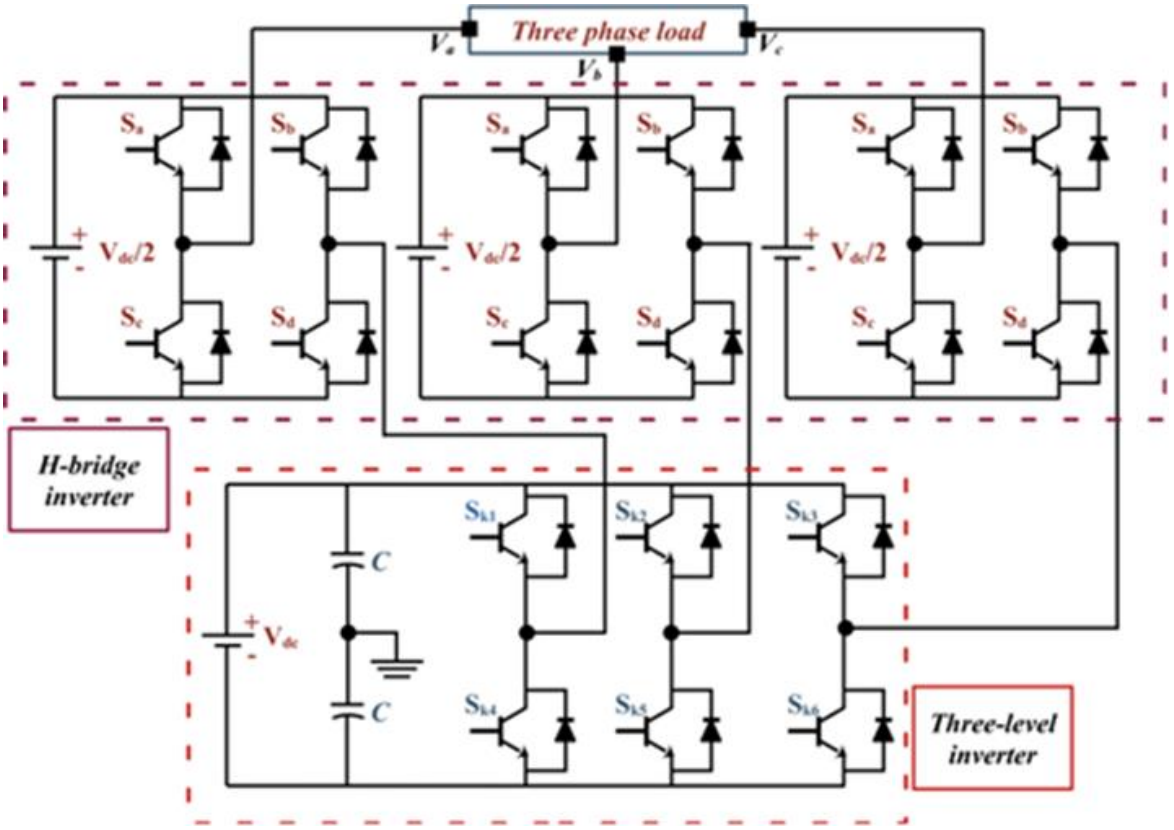

Fig. 6. The topology of the seven level three-phase cascaded H-bridge multi-level inverter

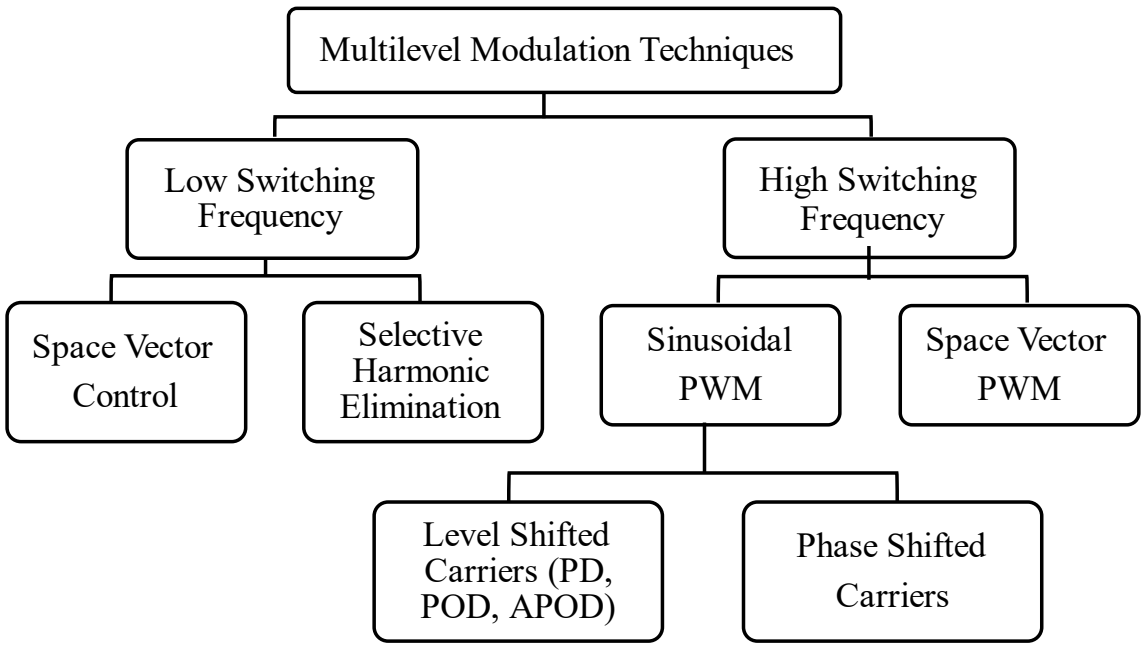

Fig. 7. Classification of modulation techniques

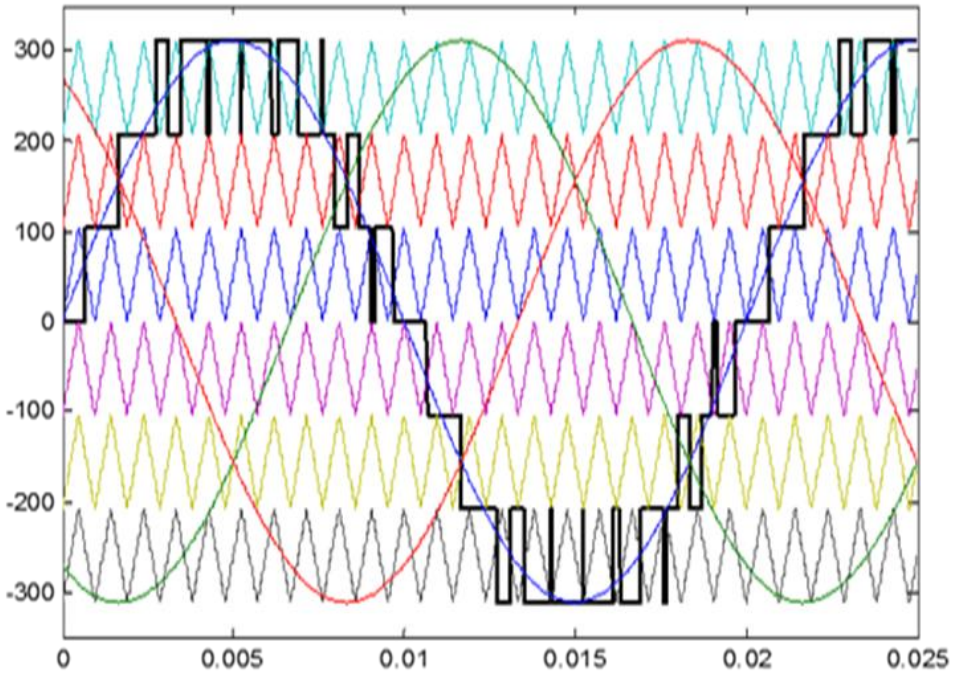

Fig. 8. Illustration of the multi-carrier PWM method, where multiple triangular carriers are compared with a sinusoidal reference signal to generate the switching pulses for a seven-level MLI. Six triangular carriers with different level and in phase are used. fc: carrier frequency = 1kHz; fm: modulation wave frequency=50Hz

4.1. Variation of Load Torque and Rotor Resistance

In this test, the DSIM initially operates under no-load conditions. To evaluate robustness, we performed tests using both the NFC and PI controller, while varying the rotor resistance (R_r) by $R_n + 50\%$ after t=1s; R_n is the nominal resistance of the rotor. At t=2s, a load of $C_r = 14\ N.m$ is applied. The test was conducted using MLI levels set to values of m=2, 5, and 7.

Fig. 9 presents the stator current per phase for different values of MLI level (m=2, 5 and 7). It can be observed that the PI controller performs worse in the case of m=2 compared to the NFC. The results clearly show that increasing the number of converter levels directly improves the sinusoidal quality of the output voltage, with higher-level converters producing waveforms that closely approximate an ideal sinusoid. Indeed, higher converter levels result in smoother waveforms because they provide more switching points within a single cycle. This allows the output voltage to more closely approximate a sinusoidal waveform, reducing harmonic distortion. The improved harmonic filtering minimizes high-frequency components, leading to a more stable current flow. Indeed, The NFC controller shows robust performance across all MLI levels.

Fig. 10 shows the evolution of the electromagnetic torque for different values of MLI level (m=2, 5 and 7) for both controllers. These results demonstrate that the PI controller is highly sensitive to harmonic distortion at low MLI levels, resulting in poor torque control and high ripple in the m = 2 case. As the inverter levels increase (m = 5 and m = 7), the PI controller's performance improves significantly due to the reduction in harmonics.

In contrast, the NFC controller shows robust performance across all MLI levels, with consistently smooth torque control, indicating its greater resilience to harmonic distortion and its ability to handle parameter variations. This can be explained by the fact that the NFC's advanced control strategy is inherently better at handling dynamic changes and adapting to harmonic distortion.

Furthermore, for m=2, there is significant overshoot and oscillation in the torque response with the PI controller. This large overshoot indicates that the PI controller struggles to handle the harmonic distortion, where the NFC controller consistently controls overshoot across all MLI levels.

4.2. Variation of Speed

In this test, the motor reference speed is changed from 1500 rpm to 2500 rpm. The other conditions remain unchanged; 50% increase in rotor resistance applied at t=1s and the application of a 14 $N.m$ load torque at t=2s. As illustrated in Fig. 11, both controllers are able to track the reference speed (W_{ref}) accurately, with minimal steady-state error. Nevertheless, the NFC controller consistently outperforms the PI controller in terms of transient response and disturbance rejection.

The NFC controller exhibits superior performance and robustness, especially in the face of constant time variations. Unlike the PI controller, which can be sensitive to such disturbances, the NFC controller maintains accurate control, highlighting its adaptability and reliability in dynamic operating conditions.

Simulation results demonstrate that the proposed NFC controller outperforms the traditional PI controller in terms of performance and robustness. The NFC effectively reduces pulsations in electromagnetic torque and stator currents, particularly when used with a multi-level inverter compared to a conventional inverter.

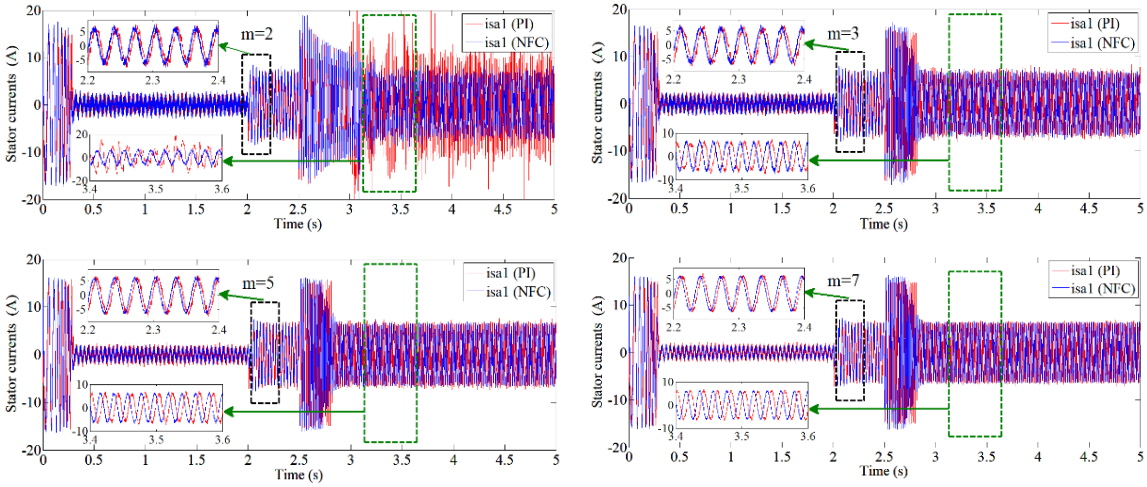

Fig. 9. Simulated responses of outputs current for different number of levels m, with increased rotor resistance (ΔRr% = +50%) followed by applying load torque (14 N.m)

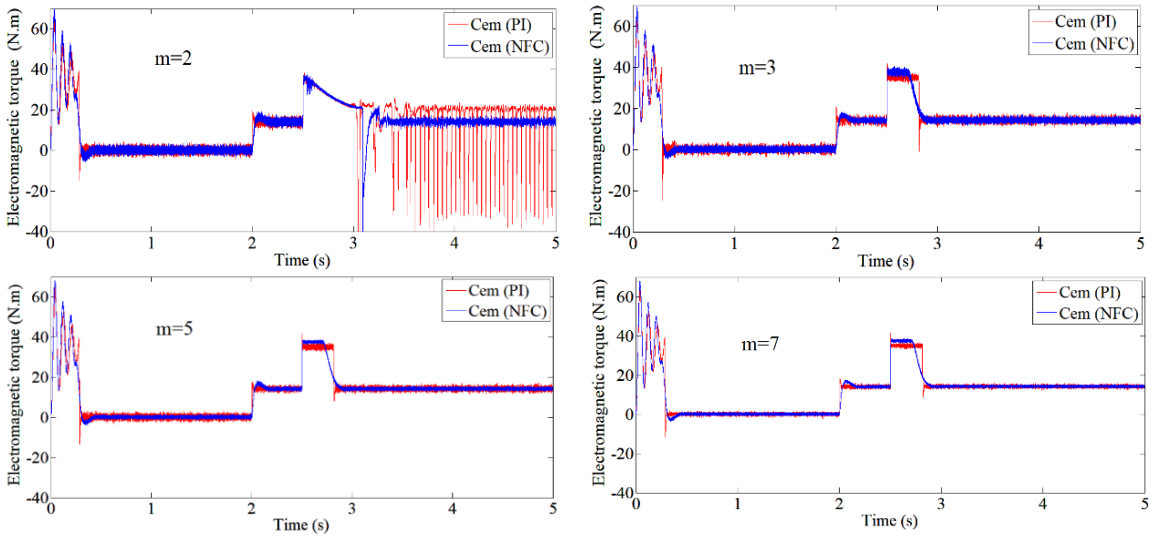

Fig. 10. Simulated responses of the electromagnetic torque for different number of levels m, with increased rotor resistance (ΔRr% = +50%) followed by applying load torque (14 N.m)

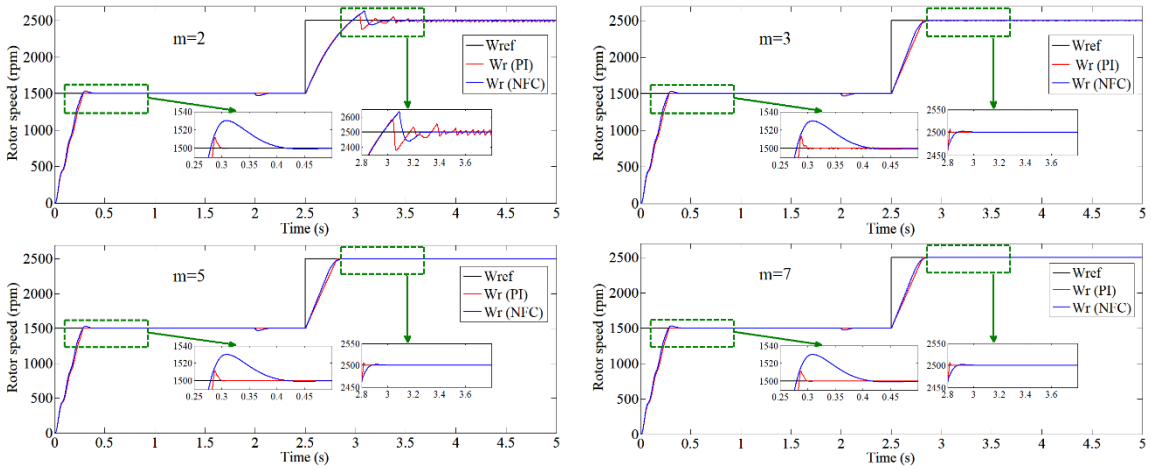

Fig. 11. Simulated responses of the rotor speed for different number of levels m with increased rotor resistance (ΔRr% = +50%) followed by applying load torque (14 N.m)

4.3. THD Performance in Normal and Degrades Modes

Table 3 compares the Total Harmonic Distortion (THD) of the current under NFC and PI controllers for different levels of MLI operation in both normal and degraded modes.

Table 3. Comparison of Current THD for NFC and PI Controllers Across Different MLI Levels in Normal and Degraded Modes

Current THD	Levels Number normally mode				Levels Number degrade mode			
	2-level	3-level	5-level	7-level	2-level	3-level	5-level	7-level
PI	5.35 %	4.66%	3.71%	2.59%	20.35 %	14.50%	9.71%	6.59%
FNC	4.25%	3.22%	2.29%	1.27%	11.67%	6.73%	4.35%	3.72%

Ii is clear that the NFC controller exhibits superior harmonic suppression capabilities in normal operation. At a 2-level MLI, the NFC reduces THD by 20% compared to the PI controller, achieving a value of 4.25%. This trend of improved performance continues at higher levels. At the 7-level MLI, the NFC significantly outperforms the PI controller, reducing THD by 51% to a value of 1.27%.

The robustness of the NFC controller becomes even more apparent under degraded operating conditions. While the THD increases for both controllers, the NFC controller maintains significantly lower values compared to the PI controller. At a 2-level MLI, the NFC reduces THD by 43% compared to the PI controller, achieving a value of 11.67%. Similarly, at the 7-level MLI, the NFC significantly outperforms the PI controller, reducing THD by 44% to a value of 3.72%.

Furthermore, for both modes, increasing the number of switching levels generally leads to a decrease in THD. This is expected as higher switching frequencies allow for better filtering of harmonics.

5. Experimental Validation

Experimental validation was conducted on a double-star induction machine at the Electrical Drives Systems Laboratory (LSEE) of the Polytechnic School (EMP). The machine, a rewired conventional three-phase asynchronous machine, was configured to match the simulation parameters (Table 4).

A dedicated test bench (Fig. 12) was used, with the double-star machine powered by two three-phase two-level voltage inverters. The DC bus voltage was derived from the three-phase mains. Sinusoidal triangular pulse width modulation was employed to control the power electronics switches at 10 kHz. A dSPACE 1104 real-time control board, running Control Desk, managed the control

process. Machine speed was monitored by a tachometer generator, while sensor cards and signal conditioning ensured accurate acquisition of currents and voltages.

Fig. 13 and Fig. 14 present experimental results from a two-level inverter system. Fig. 13 specifically focuses on the rotor speed and electromagnetic torque responses, while Fig. 14 illustrates the output currents. In both cases, the system is subjected to a 50% increase in rotor resistance (ΔRr%=+50%), and then a load torque of 6 $N.m$ is applied. A PI controller is used to regulate the system's performance.

Fig. 15 and Fig. 16 illustrate the experimental outcomes of a two-level inverter under identical conditions, employing an NFC controller. These figures depict the rotor speed, electromagnetic torque responses, and output currents.

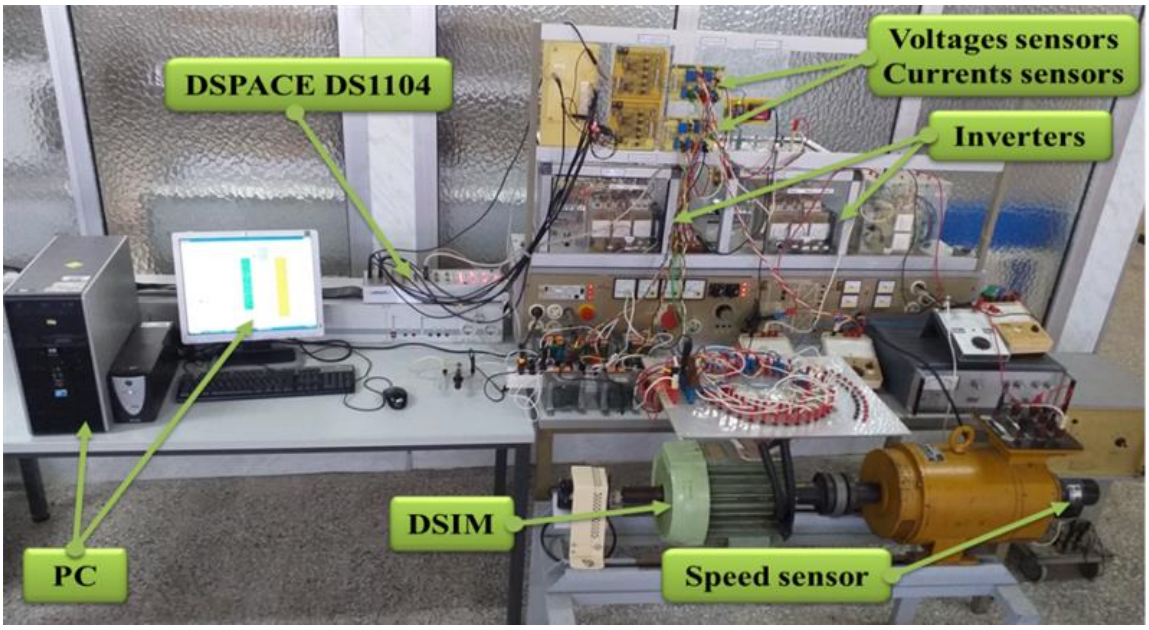

Fig. 12. Experimental test bench

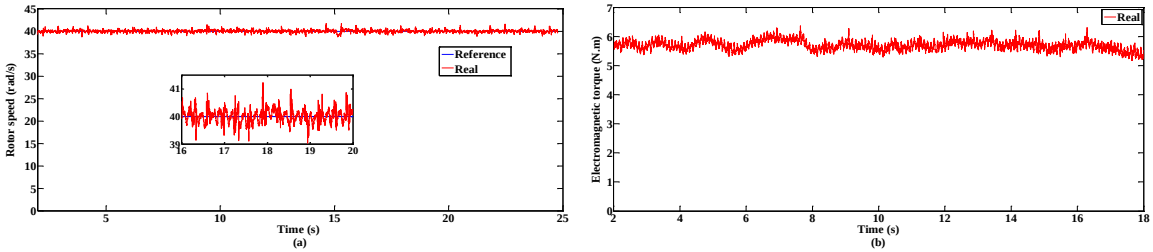

Fig. 13. Zoomed of experimental responses of rotor speed and electromagnetic torque for two levels inverters, with increased rotor resistance (ΔRr% = +50%) followed by applying load torque (6 N.m), with PI controller

It can be observed that The NFC controller provides superior control performance compared to the PI controller, offering smoother rotor speed regulation with reduced fluctuation around the reference. In fact, while the PI controller maintains rotor speed close to the reference, its deviations appear larger and more irregular than in the NFC-controlled graph. The same remark applied to the electromagnetic torque.

Due to limited lab resources, experimental validation was conducted for a two-level MLI (m=2). While this restricts the scope of our analysis, the results provide valuable insights into the system's behavior and controller performance. Future work will expand validation to higher-level MLIs as hardware becomes available.

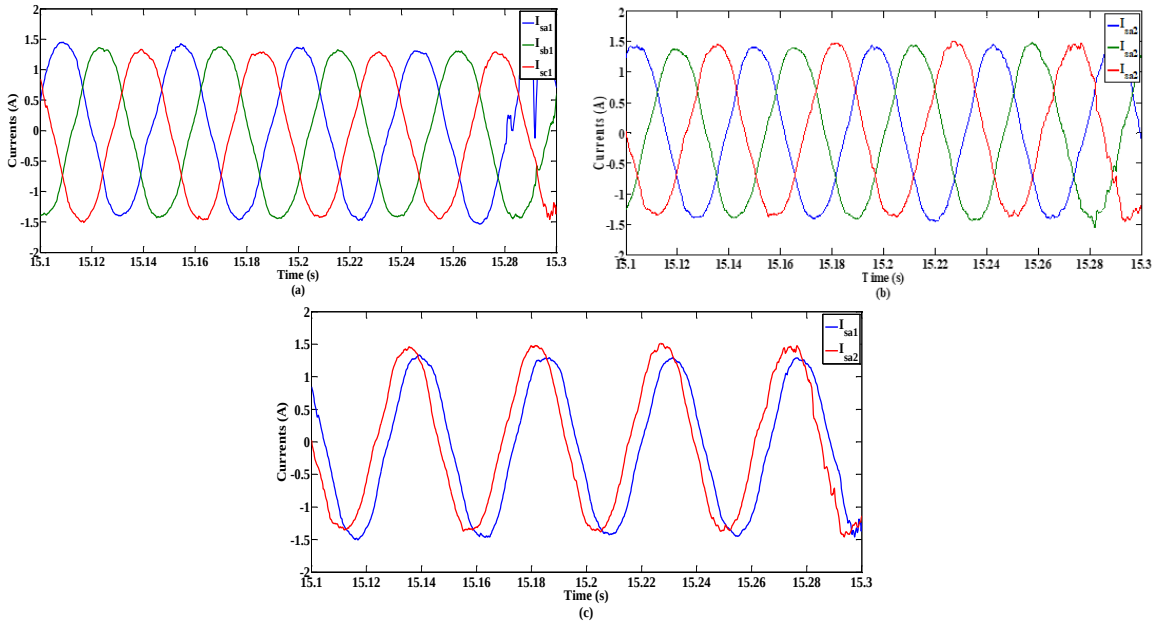

Fig. 14. Zoomed of experimental responses of outputs currents for two levels inverters, with increased rotor resistance (ΔRr% = +50%) followed by applying load torque (6N.m), with PI controller

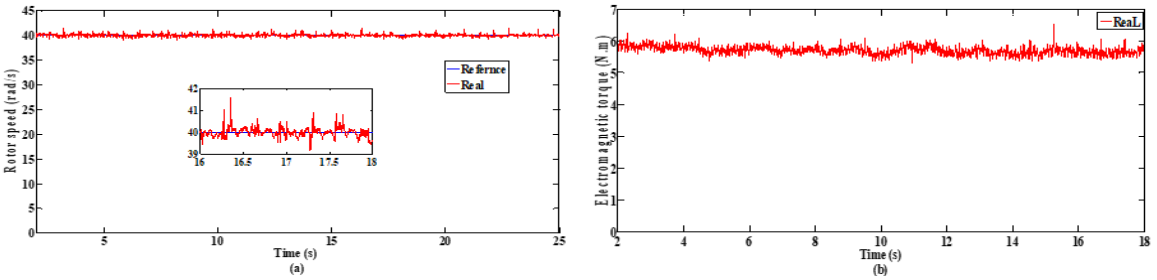

Fig. 15. Zoomed of experimental responses of rotor speed and electromagnetic torque for two levels inverters, with increased rotor resistance (ΔRr% = +50%) followed by applying load torque (6 N.m), with NFC controller

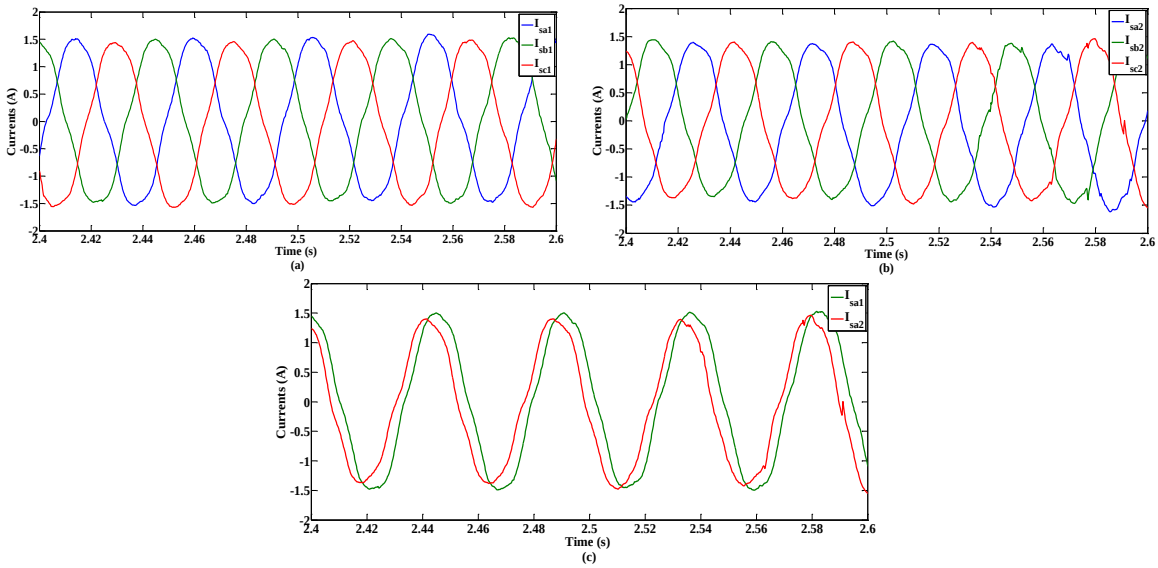

Fig. 16. Zoomed of experimental responses of outputs currents for two levels inverters, with increased rotor resistance (ΔRr%= +50%) followed by applying load torque (6N.m), with NFC controller

6. Conclusion

This study presents a NFC-based speed control system for a DSIM driven by an MLI. The proposed NFC controller demonstrates several advantages, including enhanced performance, a simple structure, robustness to disturbances, and precise speed tracking. Simulations of a DSIM powered by an MLI with a constant output voltage validate the effectiveness of the NFC.

The NFC employs a fuzzy system controller integrated with a four-layer neural network, using speed error and its derivative as inputs. Its learning process is optimized through the gradient descent technique. Simulation results clearly show the NFC's superior robustness compared to the conventional PI controller, particularly in handling various operating conditions and increasing load levels.

The primary contribution of this work is the integration of gradient descent optimization within the NFC controller, which significantly enhances its adaptability and robustness. This allows the controller to dynamically adjust its parameters in response to system variations, effectively addressing issues like harmonic distortion and parameter sensitivity, especially at lower MLI levels. The second contribution is the successful implementation of the NFC system for various MLI levels. By comparing the NFC and PI controllers, the study highlights the NFC's ability to achieve more accurate tracking, reduced fluctuations, and improved overall system stability.

Author Contribution: All authors contributed equally to the main contributor to this paper. All authors read and approved the final paper.

Funding: This research received no external funding.

Conflicts of Interest: The authors declare no conflict of interest.

Acknowledgment: We gratefully acknowledge the Electrical Drives Systems Laboratory (LSEE) of the Polytechnic School (EMP) for providing materials used for experiments for this study.

Appendix

Table 4. DSIM parameters used in simulations.

Quantity	Symbol and magnitude
Rated power Pn	4.5 kW
Rated voltage Vn	220/380 V
Rated current In	6 A
Rated speed Nn	2753 rpm
Number of poles P	2
Rated frequency f	50 Hz
Stator resistance RS	3.72 Ω
Rotor resistance Rr	2.12 Ω
Stator inductance LS	0.022 H
Rotor inductance Lr	0.006 H
Mutual inductance Lm	0.3672 H
Moment of inertia J	0.0662 kg.m2
Coefficient of viscous friction f	0.006 N.m.s/rad

References

[1] E. Zaidi *et al.*, "New PI-synergetic hybrid control for suppressing circulating currents of an electrical drive system fed by two parallel inverters," *Electrical Engineering*, 2024, https://doi.org/10.1007/s00202-024-02617-z.

[2] E. Zaidi, K. Marouani, H. Bouadi, K. Nounou, and M. Becherif, "Circulating current reduction-based hybrid controller of an electrical drive system fed by two parallel inverters," *Electrical Engineering*, vol. 103, no. 6, pp. 3049–3061, 2021, https://doi.org/10.1007/s00202-021-01284-8.

[3] S. Lekhchine, T. Bahi, and Y. Soufi, "Indirect rotor field oriented control based on fuzzy logic controlled double star induction machine," *International Journal of Electrical Power & Energy Systems*, vol. 57, pp. 206–211, 2014, https://doi.org/10.1016/j.ijepes.2013.11.053.

[4] E. Zaidi, K. Marouani, and H. Bouadi, "Speed Control for Multi-phase Induction Machine Fed by Multi-level Converters Using New Neuro-Fuzzy," *Renewable Energy for Smart and Sustainable Cities*, pp. 457–468, 2019, http://dx.doi.org/10.1007/978-3-030-04789-4_49.

[5] A. S. O. Ogunjuyigbe, T. R. Ayodele, and B. B. Adetokun, "Modelling and analysis of dual stator-winding induction machine using complex vector approach," *Engineering Science and Technology, an International Journal*, vol. 21, no. 3, pp. 351–363, 2018, https://doi.org/10.1016/j.jestch.2018.03.013.

[6] E. Levi, "Multiphase Electric Machines for Variable-Speed Applications," *IEEE Transactions on Industrial Electronics*, vol. 55, no. 5, pp. 1893–1909, 2008, https://doi.org/10.1109/TIE.2008.918488.

[7] S. Y. Yi and M. J. Chung, "Robustness of fuzzy logic control for an uncertain dynamic system," *IEEE Transactions on Fuzzy Systems*, vol. 6, no. 2, pp. 216–225, 1998, https://doi.org/10.1109/91.669018.

[8] E. Merabet, H. Amimeur, F. Hamoudi, and R. Abdessemed, "Self-Tuning Fuzzy Logic Controller for a Dual Star Induction Machine," *Journal of Electrical Engineering and Technology*, vol. 6, no. 1, pp. 133–138, 2011, https://doi.org/10.5370/JEET.2011.6.1.133.

[9] A. Oumar, R. Chakib, and M. Cherkaoui, "Current Sensor Fault-Tolerant Control of DSIM Controlled by ADRC," *Mathematical Problems in Engineering*, vol. 2020, no. 1, pp. 1-10, 2020, https://doi.org/10.1155/2020/6568297.

[10] M. Nesri, H. Benkadi, K. Nounou, G. Sifelislam, and M. F. Benkhoris, "Fault tolerant control of a dual star induction machine drive system using hybrid fractional controller," *Power Electronics and Drives*, vol. 9, no. 1, pp. 161–175, 2024, https://doi.org/10.2478/pead-2024-0010.

[11] B. Chikondra, U. R. Muduli, and R. K. Behera, "An improved open-phase fault-tolerant DTC technique for five-phase induction motor drive based on virtual vectors assessment," *IEEE Transactions on Industrial Electronics*, vol. 68, no. 6, pp. 4598–4609, 2020, https://doi.org/10.1109/TIE.2020.2992018.

[12] X. Sun, T. Li, X. Tian, and J. Zhu, "Fault-tolerant operation of a six-phase permanent magnet synchronous hub motor based on model predictive current control with virtual voltage vectors," *IEEE Transactions on Energy Conversion*, vol. 37, no. 1, pp. 337–346, 2021, https://doi.org/10.1109/TEC.2021.3109869.

[13] F. Deng, Y. Lü, C. Liu, Q. Heng, Q. Yu, and J. Zhao, "Overview on submodule topologies, modeling, modulation, control schemes, fault diagnosis, and tolerant control strategies of modular multilevel converters," *Chinese Journal of Electrical Engineering*, vol. 6, no. 1, pp. 1–21, 2020, https://doi.org/10.23919/CJEE.2020.000001.

[14] H. Mhiesan, Y. Wei, Y. P. Siwakoti, and H. A. Mantooth, "A fault-tolerant hybrid cascaded H-bridge multilevel inverter," *IEEE Transactions on Power Electronics*, vol. 35, no. 12, pp. 12702–12715, 2020, https://doi.org/10.1109/TPEL.2020.2996097.

[15] S. Rubino, O. Dordevic, R. Bojoi, and E. Levi, "Modular vector control of multi-three-phase permanent magnet synchronous motors," *IEEE Transactions on Industrial Electronics*, vol. 68, no. 10, pp. 9136–9147, 2020, https://doi.org/10.1109/TIE.2020.3026271.

[16] M. Nikpayam, M. Ghanbari, A. Esmaeli, and M. Jannati, "Fault-tolerant control of Y-connected three-phase induction motor drives without speed measurement," *Measurement*, vol. 149, p. 106993, 2020, https://doi.org/10.1016/j.measurement.2019.106993.

[17] M. Nikpayam, M. Ghanbari, A. Esmaeli, and M. Jannati, "Vector Control Methods for Star-Connected Three-Phase Induction Motor Drives Under the Open-Phase Failure," *Journal of Operation and Automation in Power Engineering*, vol. 10, no. 2, pp. 155–164, 2022, https://doi.org/10.22098/joape.2022.8802.1616.

[18] E. Zaidi, K. Marouani, H. Bouadi, A. E. Kassel, L. Bentouhami, and E. Merabet, "Fuzzy Sliding Mode Method for Speed regulation of a Dual Star Induction Machine Drive fed by Multi-level Inverters," *2018*

International Conference on Applied Smart Systems (ICASS), pp. 1–7, 2018, https://doi.org/10.1109/ICASS.2018.8651948.

[19] X. Fu and S. Li, "A Novel Neural Network Vector Control Technique for Induction Motor Drive," *IEEE Transactions on Energy Conversion*, vol. 30, no. 4, pp. 1428–1437, 2015, https://doi.org/10.1109/TEC.2015.2436914.

[20] A. G. M. A. Aziz, A. Y. Abdelaziz, Z. M. Ali, and A. A. Z. Diab, "A Comprehensive Examination of Vector-Controlled Induction Motor Drive Techniques," *Energies*, vol. 16, no. 6, p. 2854, 2023, https://doi.org/10.3390/en16062854.

[21] E. Zaidi, K. Marouani, A. E. Mabrek, E. Merabet, and L. Bentouhami, "Fuzzy Logic Control of Multi-Phase Induction Machine Drives Based on Cascaded Hybrid Multi-level Inverters," *2018 International Conference on Electrical Sciences and Technologies in Maghreb (CISTEM)*, pp. 1–6, 2018, https://doi.org/10.1109/CISTEM.2018.8613481.

[22] M. Jannati, N. Idris, and M. Aziz, "Indirect rotor field-oriented control of fault-tolerant drive system for three-phase induction motor with rotor resistance estimation using EKF," *Indonesian Journal of Electrical Engineering and Computer Science*, vol. 12, no. 9, pp. 6633–6643, 2014, http://doi.org/10.11591/ijeecs.v12.i9.pp6633-6643.

[23] M. Jannati, N. R. Nik Idris, and M. J. Abdul Aziz, "Vector control of star-connected 3-phase induction motor drives under open-phase fault based on rotor flux field-oriented control," *Electric Power Components and Systems*, vol. 44, no. 20, pp. 2325–2337, 2016, https://doi.org/10.1080/15325008.2016.1222026.

[24] M. Jannati, A. Monadi, N. R. N. Idris, and M. J. Abdul Aziz, "Experimental evaluation of FOC of 3-phase IM under open-phase fault," *International Journal of Electronics*, vol. 104, no. 10, pp. 1675–1688, 2017, https://doi.org/10.1080/00207217.2017.1321144.

[25] R. Tabasian, M. Ghanbari, and M. Jannati, "A simple method for vector control of 3-phase induction motor under open-phase fault for electric vehicle applications," *Journal of Applied Dynamic Systems and Control*, vol. 1, no. 1, pp. 1–9, 2018, https://journals.iau.ir/article_545933.html.

[26] R. Tabasian, M. Ghanbari, A. Esmaeli, and M. Jannati, "A novel direct field-oriented control strategy for fault-tolerant control of induction machine drives based on EKF," *IET Electric Power Applications*, vol. 15, no. 8, pp. 979–997, 2021, https://doi.org/10.1049/elp2.12051.

[27] S. P. A and K. Nallathambi, "An Extensive Review on Fault Detection and Fault-tolerant Control of Multilevel Inverter with Applications," *International Journal of Renewable Energy Research-IJRER*, vol. 12, no. 2, pp. 768-798, 2022, https://doi.org/10.20508/ijrer.v12i2.12586.g8465.

[28] B. Benbouya *et al.*, "Dynamic Assessment and Control of a Dual Star Induction Machine State Dedicated to an Electric Vehicle Under Short-Circuit Defect," *International Journal of Robotics and Control Systems*, vol. 4, no. 4, pp. 731-1745, 2024, https://doi.org/10.31763/ijrcs.v4i4.1557.

[29] V. Utkin, A. Poznyak, Y. Orlov, and A. Polyakov, "Conventional and high order sliding mode control," *Journal of the Franklin Institute*, vol. 357, no. 15, pp. 10244–10261, 2020, https://doi.org/10.1016/j.jfranklin.2020.06.018.

[30] A. Benabbas, E. Zaidi, and R. Abdessemed, "Sliding Mode Control of a Wind Power System Based on a Self-Excited Asynchronous Generator," *Journal Européen des Systèmes Automatisés*, vol. 55, no. 1, p. 131, 2022, https://doi.org/10.18280/jesa.550114.

[31] M. A. Fnaiech, F. Betin, Gé.-A. Capolino, and F. Fnaiech, "Fuzzy Logic and Sliding-Mode Controls Applied to Six-Phase Induction Machine With Open Phases," *IEEE Transactions on Industrial Electronics*, vol. 57, no. 1, pp. 354–364, 2010, https://doi.org/10.1109/TIE.2009.2034285.

[32] E. Zaidi, K. Marouani, H. Bouadi, K. Nounou, M. Aissani and L. Bentouhami, "Control of a Multiphase Machine Fed by Multilevel Inverter Based on Sliding Mode Controller," *2019 IEEE International Conference on Environment and Electrical Engineering and 2019 IEEE Industrial and Commercial Power Systems Europe (EEEIC/I&CPS Europe)*, pp. 1-6, 2019, https://doi.org/10.1109/EEEIC.2019.8783559.

[33] H. Ma, Y. Li, and Z. Xiong, "Discrete-Time Sliding-Mode Control With Enhanced Power Reaching Law," *IEEE Transactions on Industrial Electronics*, vol. 66, no. 6, pp. 4629–4638, 2019, https://doi.org/10.1109/TIE.2018.2864712.

[34] Y. Kali *et al.*, "Time delay estimation based discrete-time super-twisting current control for a six-phase induction motor," *IEEE Transactions on Power Electronics*, vol. 35, no. 11, pp. 12570–12580, 2020, https://doi.org/10.1109/TPEL.2020.2995773.

[35] Y. Kali, M. Saad, J. Doval-Gandoy, J. Rodas, and K. Benjelloun, "Discrete sliding mode control based on exponential reaching law and time delay estimation for an asymmetrical six-phase induction machine drive," *IET Electric Power Application*, vol. 13, no. 11, pp. 1660–1671, 2019, https://doi.org/10.1049/iet-epa.2019.0058.

[36] Y. Kali, M. Saad, J. Doval-Gandoy, and J. Rodas, "Discrete terminal super-twisting current control of a six-phase induction motor," *Energies*, vol. 14, no. 5, p. 1339, 2021, https://doi.org/10.3390/en14051339.

[37] Y. Kali, M. Saad, K. Benjelloun, and A. Fatemi, "Discrete-time second order sliding mode with time delay control for uncertain robot manipulators," *Robotics and Autonomous Systems*, vol. 94, pp. 53–60, 2017, https://doi.org/10.1016/j.robot.2017.04.010.

[38] Y. Kali *et al.*, "Current control of a six-phase induction machine drive based on discrete-time sliding mode with time delay estimation," *Energies*, vol. 12, no. 1, p. 170, 2019, https://doi.org/10.3390/en12010170.

[39] M. S. Zaky and M. K. Metwaly, "A Performance Investigation of a Four-Switch Three-Phase Inverter-Fed IM Drives at Low Speeds Using Fuzzy Logic and PI Controllers," *IEEE Transactions on Power Electronics*, vol. 32, no. 5, pp. 3741–3753, 2017, https://doi.org/10.1109/TPEL.2016.2583660.

[40] T. Bessaad, R. Taleb, F. Chabni, and A. Iqbal, "Fuzzy adaptive control of a multimachine system with single inverter supply," *International Transactions on Electrical Energy Systems*, vol. 29, no. 10, p. e12070, 2019, https://doi.org/10.1002/2050-7038.12070.

[41] N. Farah *et al.*, "A Novel Self-Tuning Fuzzy Logic Controller Based Induction Motor Drive System: An Experimental Approach," *IEEE Access*, vol. 7, pp. 68172–68184, 2019, https://doi.org/10.1109/ACCESS.2019.2916087.

[42] F. Aymen, N. Mohamed, S. Chayma, C. H. R. Reddy, M. M. Alharthi, and S. S. M. Ghoneim, "An Improved Direct Torque Control Topology of a Double Stator Machine Using the Fuzzy Logic Controller," *IEEE Access*, vol. 9, pp. 126400–126413, 2021, https://doi.org/10.1109/ACCESS.2021.3110477.

[43] S. Chandrasekaran, S. Durairaj, and S. Padmavathi, "A Performance Improvement of the Fuzzy Controller-Based Multi-Level Inverter-Fed Three-Phase Induction Motor with Enhanced Time and Speed of Response," *Journal of Electrical Engineering & Technology*, vol. 16, no. 2, pp. 1131–1141, 2021, http://dx.doi.org/10.1007/s42835-020-00649-6.

[44] T. L. Van, T. H. Nguyen, and D.-C. Lee, "Advanced Pitch Angle Control Based on Fuzzy Logic for Variable-Speed Wind Turbine Systems," *IEEE Transactions on Energy Conversion*, vol. 30, no. 2, pp. 578–587, 2015, https://doi.org/10.1109/TEC.2014.2379293.

[45] R. Sitharthan, C. Sundarabalan, K. Devabalaji, T. Yuvaraj, and A. Mohamed Imran, "Automated power management strategy for wind power generation system using pitch angle controller," *Measurement and Control*, vol. 52, no. 3–4, pp. 169–182, 2019, https://doi.org/10.1177/0020294019827330.

[46] O. A. Zabin and A. Ismael, "Rotor Current Control Design for DFIG-based Wind Turbine Using PI, FLC and Fuzzy PI Controllers," *2019 International Conference on Electrical and Computing Technologies and Applications (ICECTA)*, pp. 1–6, 2019, https://doi.org/10.1109/ICECTA48151.2019.8959530.

[47] O. Zamzoum, Y. E. Mourabit, M. Errouha, A. Derouich, and A. E. Ghzizal, "Power control of variable speed wind turbine based on doubly fed induction generator using indirect field-oriented control with fuzzy logic controllers for performance optimization," *Energy Science & Engineering*, vol. 6, no. 5, pp. 408–423, 2018, https://doi.org/10.1002/ese3.215.

[48] L. Wogi, T. Ayana, M. Morawiec, and A. Jąderko, "A comparative study of fuzzy SMC with adaptive fuzzy PID for sensorless speed control of six-phase induction motor," *Energies*, vol. 15, no. 21, p. 8183, 2022, https://doi.org/10.3390/en15218183.

[49] L. Sheng, G. Xiaojie, and Z. Lanyong, "Robust adaptive backstepping sliding mode control for six-phase permanent magnet synchronous motor using recurrent wavelet fuzzy neural network," *IEEE Access*, vol. 5, pp. 14502–14515, 2017, https://doi.org/10.1109/ACCESS.2017.2721459.

[50] M. Benakcha, L. Benalia, D. E. Tourqui, and A. Benakcha, "Backstepping control of dual stator induction generator used in wind energy conversion system," *International Journal of Renewable Energy Research*, vol. 8, no. 1, pp. 384–395, 2018, https://doi.org/10.20508/ijrer.v8i1.7025.g7313.

[51] M. Morawiec, P. Strankowski, A. Lewicki, J. Guziński, and F. Wilczyński, "Feedback control of multiphase induction machines with backstepping technique," *IEEE Transactions on Industrial Electronics*, vol. 67, no. 6, pp. 4305–4314, 2020, https://doi.org/10.1109/TIE.2019.2931236.

[52] H. Echeikh, R. Trabelsi, H. Kesraoui, A. Iqbal, and M. Mimouni, "Torque ripples improvement of direct torque controlled five-phase induction motor drive using backstepping control," *International Journal of Power Electronics and Drive Systems (IJPEDS)*, vol. 11, no. 1, pp. 64-74, 2020, http://doi.org/10.11591/ijpeds.v11.i1.pp64-74.

[53] C. Berrahal, A. E. Fadili, F. Giri, A. E. Magri, R. Lajouad, and I. E. Myasse, "Robustness of Backstepping Multiphase Induction Machine Control in Presence of Open Phases Fault," *IFAC-PapersOnline*, vol. 55, no. 12, pp. 794–799, 2022, https://doi.org/10.1016/j.ifacol.2022.07.410.

[54] F.-J. Lin, S.-G. Chen, and C.-W. Hsu, "Intelligent Backstepping Control Using Recurrent Feature Selection Fuzzy Neural Network for Synchronous Reluctance Motor Position Servo Drive System," *IEEE Transactions on Fuzzy Systems*, vol. 27, no. 3, pp. 413–427, 2019, https://doi.org/10.1109/TFUZZ.2018.2858749.

[55] F. Beltran-Carbajal, H. Yañez-Badillo, D. Galvan-Perez, I. Rivas-Cambero, D. Sotelo, and C. Sotelo, "B-Spline Artificial Neural Networks in Robust Induction Motor Control," *IEEE Access*, vol. 12, pp. 101679–101700, 2024, https://doi.org/10.1109/ACCESS.2024.3430323.

[56] B. Kiran Kumar, Y. V. Siva Reddy, and M. Vijaya Kumar, "Neuro Fuzzy Controller for DTC of Induction Motor Using Multilevel Inverter with SVM," *Journal of Circuits, Systems and Computers*, vol. 30, no. 14, p. 2150250, 2021, https://doi.org/10.1142/S0218126621502509.

[57] T. H. dos Santos, A. Goedtel, S. A. O. da Silva, and M. Suetake, "Scalar control of an induction motor using a neural sensorless technique," *Electric Power Systems Research*, vol. 108, pp. 322–330, 2014, https://doi.org/10.1016/j.epsr.2013.11.020.

[58] F. Kadri and M. A. Hamida, "Neural Direct Torque Control for Induction Motor under Voltage Source Inverter Open Switch Fault," *Recent Advances in Electrical & Electronic Engineering*, vol. 13, no. 4, pp. 571–579, 2020, http://dx.doi.org/10.2174/1874476105666190830103616.

[59] A. K. Awasthi, R. T. Ugale, and A. Kumar, "ANN Based Robust control of Linear Induction Motor," *IECON 2020 The 46th Annual Conference of the IEEE Industrial Electronics Society*, pp. 870–875, 2020, https://doi.org/10.1109/IECON43393.2020.9255408.

[60] B. Desalegn, D. Gebeyehu, and B. Tamrat, "Smoothing electric power production with DFIG-based wind energy conversion technology by employing hybrid controller model," *Energy Reports*, vol. 10, pp. 38–60, 2023, https://doi.org/10.1016/j.egyr.2023.06.004.

[61] D. Hadiouche, H. Razik, and A. Rezzoug, "On the modeling and design of dual-stator windings to minimize circulating harmonic currents for VSI fed AC machines," *IEEE Transactions on Industry Applications*, vol. 40, no. 2, pp. 506–515, 2004, https://doi.org/10.1109/TIA.2004.824511.

[62] E. Zaidi, K. Marouani, and H. Bouadi, "Simulation and Analysis of DSIM Speed Control System Supplied by Multi-Level Converter Using Fuzzy Logic Controller," *2019 International Conference on Advanced Electrical Engineering (ICAEE)*, pp. 1-6, 2019, https://doi.org/10.1109/ICAEE47123.2019.9015153.

[63] Z. Said and M. Abdelhafidh, "Current sensor fault tolerant control of a double star induction motor DSIM using fuzzy sliding control," *2023 International Conference on Electrical Engineering and Advanced Technology (ICEEAT)*, pp. 1-6, 2023, https://doi.org/10.1109/ICEEAT60471.2023.10426182.

[64] L. Youb, S. Belkacem, F. Naceri, M. Cernat, and L. G. Pesquer, "Design of an adaptive fuzzy control system for dual star induction motor drives," *Advances in Electrical and Computer Engineering*, vol. 18, no. 3, pp. 37–44, 2018, http://dx.doi.org/10.4316/AECE.2018.03006.

[65] K. Hamitouche, S. Chekkal, H. Amimeur, and D. Aouzellag, "A new control strategy of dual stator induction generator with power regulation," *Journal Européen des Systèmes Automatisés*, vol. 53, no. 4, pp. 469–478, 2020, https://doi.org/10.18280/jesa.530404.

[66] L. Hellali and B. Saad, "Speed control of doubly star induction motor (DSIM) using direct field oriented control (DFOC) based on fuzzy logic controller (FLC)," *Advances in Modelling and Analysis C*, vol. 73, pp. 128–136, 2018, https://doi.org/10.18280/ama_c.730402.

[67] L. Bentouhami, R. Abdessemed, A. Kessal, and E. Merabet, "Control Neuro-Fuzzy of a Dual Star Induction Machine (DSIM) supplied by Five-Level Inverter," *Journal of Power Technologies*, vol. 98, no. 1, pp. 70–79, 2018, http://dx.doi.org/10.4236/jpt.2018.63001.

[68] F. Z. Peng, J.-S. Lai, J. W. McKeever, and J. VanCoevering, "A multilevel voltage-source inverter with separate DC sources for static VAr generation," *IEEE Transactions on Industry Applications*, vol. 32, no. 5, pp. 1130–1138, 1996, https://doi.org/10.1109/28.536875.

[69] J. Rodriguez, S. Bernet, P. K. Steimer, and I. E. Lizama, "A Survey on Neutral-Point-Clamped Inverters," *IEEE Transactions on Industrial Electronics*, vol. 57, no. 7, pp. 2219–2230, 2010, https://doi.org/10.1109/TIE.2009.2032430.

[70] T. A. Meynard and H. Foch, "Multi-level conversion: high voltage choppers and voltage-source inverters," *PESC '92 Record. 23rd Annual IEEE Power Electronics Specialists Conference*, vol. 1, pp. 397-403, 1992, https://doi.org/10.1109/PESC.1992.254717.

[71] S. Choudhury, M. Bajaj, T. Dash, S. Kamel, and F. Jurado, "Multilevel Inverter: A Survey on Classical and Advanced Topologies, Control Schemes, Applications to Power System and Future Prospects," *Energies*, vol. 14, no. 18, p. 5773, 2021, https://doi.org/10.3390/en14185773.

[72] V. Nair R., A. Rahul S., R. S. Kaarthik, A. Kshirsagar, and K. Gopakumar, "Generation of Higher Number of Voltage Levels by Stacking Inverters of Lower Multilevel Structures With Low Voltage Devices for Drives," *IEEE Transactions on Power Electronics*, vol. 32, no. 1, pp. 52–59, 2017, https://doi.org/10.1109/TPEL.2016.2528286.

[73] S. A. Khan *et al*., "Topology, Modeling and Control Scheme for a new Seven-Level Inverter With Reduced DC-Link Voltage," *IEEE Transactions on Energy Conversion*, vol. 36, no. 4, pp. 2734-2746, 2021, https://doi.org/10.1109/TEC.2021.3075964.